

# Phase Retrieval using Conditional Generative Adversarial Networks

Tobias Uelwer<sup>1</sup>, Alexander Oberstraß<sup>1</sup>, and Stefan Harmeling<sup>1</sup>

<sup>1</sup>*Department of Computer Science, Heinrich-Heine-Universität Düsseldorf, Germany*  
 {tobias.uelwer, alexander.oberstrass, harmeling}@hhu.de

## Abstract

In this paper, we propose the application of conditional generative adversarial networks to solve various phase retrieval problems. We show that including knowledge of the measurement process at training time leads to an optimization at test time that is more robust to initialization than existing approaches involving generative models. In addition, conditioning the generator network on the measurements enables us to achieve much more detailed results. We empirically demonstrate that these advantages provide meaningful solutions to the Fourier and the compressive phase retrieval problem and that our method outperforms well-established projection-based methods as well as existing methods that are based on neural networks. Like other deep learning methods, our approach is very robust to noise and can therefore be very useful for real-world applications.

## 1 Introduction

Phase retrieval is an important problem which has applications e.g. in X-ray crystallography [25], astronomical imaging [6], microscopy [35] and many more. For the sake of readability we only define the phase retrieval problems for the one-dimensional case. The extension to higher dimensions is straight forward.

**The Compressive Phase Retrieval Problem:** The compressive phase retrieval problem [27] can be defined as recovering a signal  $x \in \mathbb{R}^n$  given  $m$  measurements  $y \in \mathbb{R}^m$ , where the dependence of the measurements on the signal is described by

$$y = |Ax| =: f(x) \text{ for } A \in \mathbb{C}^{m \times n}. \quad (1)$$

The matrix  $A$  is usually called the measurement matrix.

**The Fourier Phase Retrieval Problem:** Having  $A$  as the symmetric Fourier transformation matrix  $\mathcal{F}$ , containing the primitive roots of unity, results in the Fourier phase retrieval problem, which thus can be seen as a special case of the compressive phase retrieval problem. Since the Fourier phase retrieval problem has more relevance in practice, we want to focus on this problem.

Both phase retrieval problems are highly ill-posed. As a result, prior knowledge about the signal  $x$  becomes very useful for the reconstruction process.

**Prior Work:** In practice, traditional projection-based methods like the Gerchberg-Saxton algorithm [8] or the hybrid-input-output algorithm [7] require the magnitudes of the Fourier measurements to be oversampled [17], as demonstrated in Figure 1. The influence of oversampling on the Fourier phase retrieval problem is discussed in [24]. Without oversampling, more prior knowledge about the signal is needed. Traditional methods, however, merely take some handcrafted prior information like signal sparsity into the reconstruction

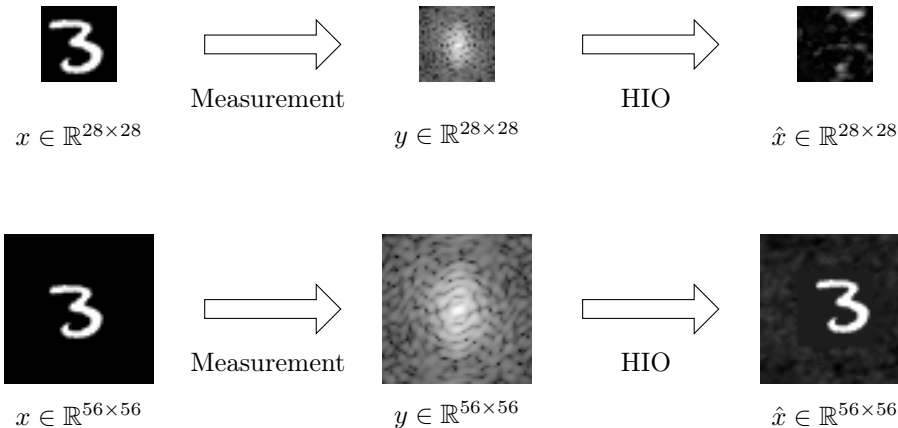


Figure 1: Reconstructing a signal with a known zero padding leading to oversampling is easier. However without padding the commonly used Hybrid-Input-Output algorithms fails to reconstruct the image.

process. Sparse phase retrieval has been discussed in [14, 30, 3, 5]. Neural networks allow the inclusion of self-learned prior knowledge and thus can be used to remedy this problem. Phase retrieval using generative models has been previously suggested by Hand et al. [10]. We describe their approach briefly in Section 2.2. Furthermore, neural networks have been used to improve the results of existing approaches: Metzler et al. [23] apply the regularization-by-denoising framework to the phase retrieval problem, where a denoising neural networks is used to construct a regularization term. Also Işıl et al. [12] used neural networks to remove artifacts that are produced during the iterations of the hybrid-input-output algorithm. Both of these approaches were only introduced for the oversampled case. Conditional generative adversarial networks have previously been applied to Fourier ptychography by Boominathan et al. [1]. Fourier ptychography is a related but different problem than the one we aim to solve.

## 2 Methods

### 2.1 End-to-End Approaches

As a baseline we use a neural network generator  $G$ , trained to directly output an approximate reconstruction  $\hat{x}$  of the input signal  $x$  by the magnitudes  $y$ :

$$\hat{x} = G(y) \quad (2)$$

In training, we optimize the distance between the original signal  $x$  and the reconstruction  $\hat{x}$ , where we construct the input measurements  $y$  by applying Equation 1 on the test samples  $x$ . However, when optimizing the Euclidean distance the reconstructed images tend to be blurry. A similar observation has been made in the context of image inpainting by Pathak et al. [28]. Therefore, we use the mean absolute error for training, which produces slightly less blurry reconstructions. To our surprise, this simple approach performs very well on our test data. We refer to the method as E2E.

### 2.2 Phase Retrieval Using a Generative Prior

Instead of directly performing optimization on the input signal  $x$  itself which was for example done by Candes et al. [4] Hand et al. [10] suggest viewing the problem through the lens of a generative model  $G$ , i.e., by optimizing its latent variable

$$z^* = \arg \min_z \|y - |AG(z)|\|_2^2. \quad (3)$$

This allows incorporating the prior knowledge of the generative model  $G$  that has been previously trained on data similar to the signal of interest. This optimization problem is solved using a modified gradient descent algorithm that accounts for solutions corresponding to latent variables having a flipped sign. Furthermore, the optimization result strongly depends on the initialization of the latent variable  $z$  and often gets stuck in local minima, as we observed for the Fourier phase retrieval problem. In practice, we found that the dimension of the latent variable  $\dim(z)$  must be chosen sufficiently small to reduce the distance  $\|y - |AG(z)|\|_2^2$  far enough. Finding an optimal point  $z^*$  with Equation 3 results in the estimated signal  $\hat{x}$  by

$$\hat{x} = G(z^*). \quad (4)$$

Throughout the paper we denote this method as DPR.

### 2.3 Conditional Generative Adversarial Networks

As our contribution, we employ a conditional GAN approach which was proposed by Goodfellow et al. [9] and Mirza and Osindero [26]. The conditional GAN has later been applied to image-to-image translation problems by Isola et al. [13]. In the following we denote the distribution of the latent variable  $z$  by  $q$ , whereas we denote the unknown data distribution by  $p$ . Although the latent distribution can be chosen arbitrarily, we stick to the standard normal distribution which is the default choice for GAN training. We found that we could use a much higher dimension for  $z$  compared to DPR and chose  $\dim(z) = \dim(y)$ . The training objective for the generator  $G$  and the discriminator  $D$  consists of an adversarial component

$$\mathcal{L}_{\text{adv}}(D, G) = \mathbb{E}_{x \sim p} [\log D(x, y)] + \mathbb{E}_{x \sim p, z \sim q} [\log (1 - D(G(z, y), y))], \quad (5)$$

where

$$y = |Ax| \quad (6)$$

and a reconstruction component

$$\mathcal{L}_{\text{rec}}(G) = \|x - G(z, y)\|_1. \quad (7)$$

The adversarial component encourages the generator to output realistic and sharp images, whereas the reconstruction guides the generator in the right direction. The optimization problem that is solved during training is given by:

$$\min_G \max_D \mathcal{L}_{\text{adv}}(D, G) + \lambda \mathcal{L}_{\text{rec}}(G), \quad (8)$$

where the hyperparameter  $\lambda$  can be used to control the influence of both losses. Because of stability issues we also used the modified GAN loss that was suggested by Goodfellow et al. [9]. We also trained the conditional GAN using the least squares objective proposed by Mao et al. [21], but we did not find the results to be better than with the logarithmic loss function as stated in Equation 5. Samples generated by

$$\hat{x} = G(z, y), \text{ with } z \sim \mathcal{N}(0, 1) \quad (9)$$

already lead to decent approximations  $\hat{x}$  of the original signal  $x$ . However, to further improve the results at test time, we adapt the method from Hand et al. [10] to seek for the optimal latent variable  $z^*$  for each data point that minimizes the squared Euclidean error of the magnitudes:

$$z^* = \arg \min_z \|y - |AG(z, y)|\|_2^2. \quad (10)$$

After the optimization of the latent variable  $z$ , the estimate of the signal is given by

$$\hat{x} = G(z^*, y) \quad (11)$$

During training, the network learns small values for the filter of the latent variable, i.e., it learns to ignore the noise. This requires us to employ large learning rates for the latent optimization during test time. Mathieu et al. [22] and Isola et al. [13] made a similar observation and removed the latent variable. Isola et al. [13] introduced additional stochasticity into the model by applying dropout during training time and testing time. However, none of these approaches yielded better results in our experiments.

In the following we refer to our approach as PRCGAN (Phase Retrieval using Conditional Generative Adversarial Network). Furthermore, we denote the PRCGAN with latent space optimization by PRCGAN\*.

### 3 Experiments: Fourier Phase Retrieval

In this section we want to empirically rate the quality of the predictions generated by the proposed method from Section 2.

**Datasets:** Commonly used datasets in deep learning are MNIST [18], Fashion-MNIST [33] and CelebA [19]. Images from MNIST and Fashion-MNIST both have the same shape of  $28 \times 28$  pixels with only one greyscale channel. They both provide 60 000 training and 10 000 test samples. For computational reasons, we reduced the test size to 1024 samples. Fashion-MNIST has more variance in the image representations which makes it harder to memorize significant patterns for our generative models. Therefore, we consider it as a harder dataset for phase retrieval than MNIST. As a third dataset, we took the popular CelebA dataset [19] consists of 202 599 face images from 10 177 different people. We took the first 162 769 images as training data, the next 19 867 as validation data and from the remaining images we took the first 1024 for evaluation. To reduce the size of the high resolution images to more computational friendly sizes, we took a center crop of  $108 \times 108$  pixels from each image and then resized it to a total scale of  $64 \times 64$  pixels. This transformation is equivalent to the one used by Hand et al. [10]. A difference of CelebA to the previously introduced datasets is that it consists of three color channels. During the measurement process, we treated each channel independently and, in the case of Fourier measurements, we performed a 2D Fourier transform for each channel separately.

**Evaluation:** To evaluate the performance of the models, we compare the distance of the reconstruction  $\hat{x}$  to the original signal  $x$ . For this we use the mean squared error (MSE), mean absolute error (MAE) and structural similarity (SSIM) [32]. These metrics do not take visual aspects like sharpness into account [31]. Especially the mean squared error tends to prefer blurry predictions.

Since the Fourier measurements are invariant under signal translation and rotation by 180 degrees, we sometimes observed these transformations in our reconstruction results as well. Although we consider these reconstructions as equally correct solutions, pixel-wise metrics like MSE do not take this property of the Fourier transformation into account. We therefore used a cross-correlation based image registration technique [2] to estimate the most probable translation by the predicted signal  $\hat{x}$  relative to the original signal  $x$ . The coordinate of strongest cross-correlation between  $x$  and  $\hat{x}$  gave us the relative translation  $(\Delta s, \Delta t)$  and could be reverted accordingly:

$$(\Delta s, \Delta t) = \arg \max_{(s,t)} \{x \star \hat{x}\}$$

where  $\star$  denotes the circular cross-correlation. After doing the same with the 180 degree rotation of  $\hat{x}$ , we took the result with minimal error from these two. In the following we only report evaluation metrics based on the registered predictions for MNIST and Fashion-MNIST. On CelebA the registration had no effect, since the images are not surrounded by zero values, as with the other datasets.

#### 3.1 MNIST and Fashion-MNIST

**HIO:** We ran 1000 iterations of the hybrid-input-output algorithm, where we set the hyperparameter  $\beta = 0.8$  with three random restarts. We did not zero-pad the original signal and reported the test error of the reconstruction  $\hat{x}$  with the lowest measurement error  $\| |A\hat{x}| - y \|_2$ .

**RAAR:** We ran 1000 iterations of the RAAR algorithm with  $\beta = 0.87$ , as it was reported to be the best choice for  $\beta$  by Luke [20]. To overcome very bad starting points, we took the best out of three random initializations.

Dataset	Metric	HIO	RAAR	E2E	DPR	PRCGAN	PRCGAN*
MNIST	MSE	0.0441	0.0489	0.0183	0.0093	0.0168	<b>0.0010</b>
	MAE	0.1016	0.1150	0.0411	0.0221	0.0399	<b>0.0043</b>
	SSIM	0.5708	0.5232	0.8345	0.9188	0.8449	<b>0.9898</b>
Fashion-MNIST	MSE	0.0646	0.0669	0.0128	0.0280	0.0151	<b>0.0087</b>
	MAE	0.1604	0.1673	0.0526	0.0856	0.0572	<b>0.0412</b>
	SSIM	0.4404	0.4314	0.7940	0.6602	0.7749	<b>0.8580</b>
CelebA	MSE	0.0737	0.0729	0.0106	0.0388	0.0138	<b>0.0093</b>
	MAE	0.2088	0.2073	0.0699	0.1323	0.0804	<b>0.0642</b>
	SSIM	0.1671	0.2274	0.7444	0.5299	0.6799	<b>0.7631</b>

Table 1: Evaluation results for MNIST, Fashion-MNIST and CelebA for the reconstructions from the Fourier magnitudes. We register the reconstructions for MNIST and Fashion-MNIST. MSE, MAE: lower is better. SSIM: higher is better.

**End-to-End (E2E):** For the end-to-end (E2E) approach, we used the same structure for a generator  $G(y)$ , where  $y$  denotes the measurement information, with 5 fully connected layers of sizes  $784 - 2048 - 2048 - 2048 - 784$  for both datasets. We preferred using fully-connected layers over convolutional layers to match the property of each measurement depending on every image pixel and vice versa. This assumption was consistent with our observation that fully-connected networks performed slightly better over pure convolutional networks in practice. As input at train and test time, we took the measurement information  $y$  for each data sample by applying Equation 1 and flattened it to a vector of size 784 to feed the first fully-connected layer. This first layer then mapped the input vector to a hidden size of 2048. The last layer mapped the 2048 hidden values back again to 784 pixel values that were then rearranged to a  $28 \times 28$  image output again. We placed batch-normalization [11] and ReLU activations in between all fully-connected layers. The output of the last layer was then passed to a Sigmoid function to ensure the output was in the range  $[0, 1]$ .

**DPR:** As generative model  $G$  for the generative prior approach we used a Variational autoencoder (VAE) [16] similar to the one proposed by Hand et al. [10], but we had more success with a higher dimension of 128 for of the latent space  $z$  in the Fourier measurement case. Therefore, our decoder network got the size of  $128 - 500 - 500 - 784$  (with the encoder vice versa). While this choice of model size resulted in 10 times fewer learnable parameters than the comparable E2E and PRCGAN approaches, we did not observe any improvement in performance when using a larger model. For larger models, the results even got worse slightly.

After training the VAE, we performed the optimization steps as described in Section 2.2 for a random initialization  $z \sim \mathcal{N}(0, 1)$  to find an optimal  $z^*$  and recorded  $G(z^*)$ . We ran 10 000 optimization steps with a learning rate of 0.1 and the Adam optimizer [15], which we found performed best among several optimization strategies. The vanilla stochastic gradient descent (SGD) did not work at all. Since the optimization often got stuck in local minima depending on the initialization of the latent space, we recorded only the best out of three random restarts.

**PRCGAN:** To keep the approaches comparable, we took the same model structure as for the E2E case but with a twice as high input size for the additional latent noise  $z$ , resulting in a generator  $G$  with sizes  $1568 - 2048 - 2048 - 2048 - 2048 - 784$ . During training we found the choice of hyperparameter  $\lambda = 1000$  performed best. Lower values resulted in artifacts like scattered dots throughout the image. Higher values led to blurred results, which is consistent with the outcomes of the E2E approach. The outputs only based on the conditional information with random latent noise initialization of  $z$  already produced reasonable results.

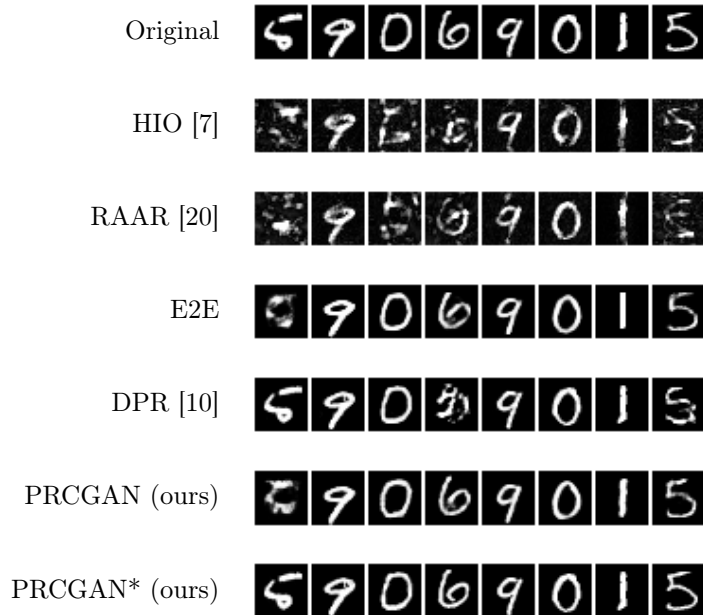


Figure 2: Registered reconstructions from the Fourier magnitudes of samples from the MNIST test dataset for each model.

After training, we did perform the same amount of optimization steps as for the DPR approach to solve Equation 10 to find an optimal latent variable  $z^*$ . However, we were required to use a much higher learning rate for this model. This is caused by the small weights for latent variable learned during training. The high learning rate overcame this problem and produced even better results with the optimized latent variable  $z^*$  than the results with random  $z$ .

**Results:** Table 1 summarizes the evaluation results for various metrics on the full 1024 sample test sets. Figures 2 and 3 show a comparison of the reconstruction of the first eight test samples from the MNIST and Fashion-MNIST datasets. The first lines show the original ground truth. Traditional methods like HIO and RAAR are not able to converge to the correct solution, resulting in fragmented, blurry outputs on both datasets. While the E2E approach overcomes the problem of constructing fragmented parts, it still tends to produce blurry outputs. Due to the adversarial loss component, the PRCGAN approach begins to paint finer texture components like the text on the sweatshirt in the second sample and the check pattern on the shirt in the eighth sample shown in Figure 3. While on MNIST the numerical results are consistent with this observation, our evaluation metrics rate the E2E better in the case of Fashion-MNIST than the PRCGAN as shown in Table 1 because they do not take these visual aspects into account and prefer a risk minimized output without the risk of misplaced sharp edges.

On MNIST, the approaches with latent optimization, DPR and PRCGAN\*, produce the best visual appearance of the digits among all approaches. However, DPR is getting stuck in local minima sometimes, as one can see from the fourth and eighth test sample in Figure 2. With other random initializations these samples got reconstructed perfectly, but we only allowed three random restarts to keep the computational effort limited. The numerical results in Table 1 also show that DPR and PRCGAN\* perform best on MNIST, while the PRCGAN\* performed even better because it is not affected by local minima in the optimization landscape.

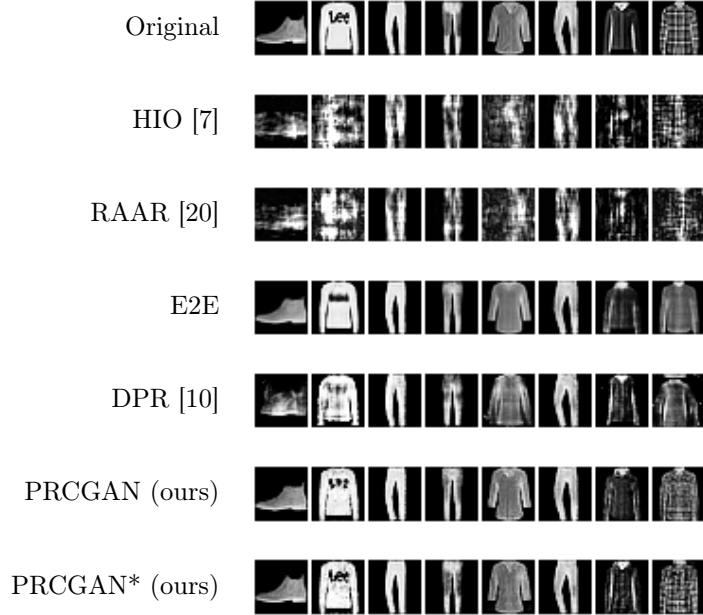


Figure 3: Registered reconstructions from the Fourier magnitudes of samples from the Fashion-MNIST test dataset for each model.

On the Fashion dataset, the rating of DPR drops dramatically. The outputs become even more random than on MNIST. It falls back behind all other deep learning approaches. While PRCGAN\* still performs best, its advantage over the other methods becomes smaller. However, it is remarkable that this is the only approach producing a readable variant of the text on the sweatshirt in the second sample in Figure 3.

**Robustness to Noise:** To train our PRCGAN, we create synthetic noiseless measurements. However, real experiments contain several sources of noise that can disrupt the reconstruction process. In this section we show that our model, as other deep learning approaches, is still very robust to noise.

Experiments often measure intensities as the squared Fourier magnitudes through discrete photon counting, as performed in X-ray crystallography [5], resulting in additive noise

$$\hat{y}^2 = y^2 + w \quad (12)$$

for the measured intensities  $\hat{y}^2$  consisting of the true intensities  $y^2$  and noise  $w$ . Shot noise is one of the dominant sources of noise for photon counts [34] and is used by Metzler et al. [23] to show robustness to noise. They suggest attaining the noisy magnitudes  $\hat{y}$  by sampling

$$s \sim \text{Poisson} \left( \frac{y^2}{\alpha^2} \right) \quad (13)$$

$$\hat{y} = \alpha \sqrt{s}$$

where  $\alpha$  controls the variance of the random variable  $\hat{y}^2$  and therefore the signal to noise ratio (SNR). However, the variance additionally depends on the scale of the true magnitudes  $y$  that can differ between experimental setups. Therefore, we also measured the SNR of the noisy model input  $\hat{y}$  directly for each sample by

$$\text{SNR} = \frac{\mu_{\text{magn}}}{\sigma_{\text{noise}}} \quad (14)$$

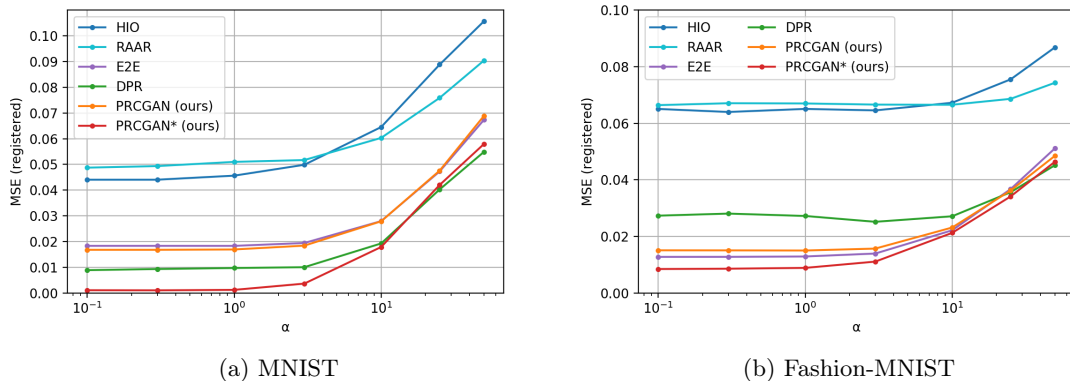


Figure 4: MSE of registered reconstructions from noisy Fourier magnitudes from the MNIST and Fashion-MNIST datasets.  $\alpha$  controls the noise level. Higher  $\alpha$  corresponds to stronger noise.

where  $\mu_{\text{magn}}$  denotes the mean of the true magnitudes  $y$  and  $\sigma_{\text{noise}}$  the standard deviation of the error  $\hat{y} - y$ .

Figure 4 shows the reconstruction results for the proposed methods as the mean MSE for different values of  $\alpha$  on the MNIST and Fashion-MNIST datasets for each 1024 samples. Both plots show that we are robust to noise up to  $\alpha = 3$  related to  $\text{SNR} \approx 3$ . All deep learning approaches show similar robustness to noise. The slight leading and unexpected observed improvement of the DPR in the high variance regions we attribute to the 3 allowed random restarts that increase their impact the more random the outputs get.

### 3.2 CelebA

**E2E:** The flattened version of images from CelebA, as we did for the fully-connected models for MNIST and Fashion-MNIST, would result in a 12 288 dimensional input vector for the CelebA dataset. Since this would lead to very huge matrices within the fully-connected layers, they were not suitable enough anymore. To still fulfill the property of global dependence of each measurement on the signal for the generator, we first compressed the input for the E2E model by five convolutional layers. After the last convolutional layer the input had a flattened size of 2048. We then could append two fully-connected layers with moderate computational effort, preserving the dimension of 2048. The output of the fully-connected layers was then upsampled to the full image size by five transposed convolutional layers again. The output of the last layers was then passed to a Sigmoid function to ensure the output of the network was in the range  $[0, 1]$ . We used batch-normalization and ReLU activation between all layers.

**DPR:** As a generative model we used a DCGAN [29] which we trained for 100 epochs. Similar to the DPR optimization for MNIST and Fashion-MNIST, we ran 10 000 optimization steps with a learning rate of 0.1 and the Adam optimizer to find an optimal latent variable  $z^*$ . Again, we gave the DPR approach three restarts for different random initializations and only recorded the best result.

**PRCGAN:** To get comparable results, we used the same model structure as for the E2E approach with additional three channels for a additional  $3 \times 64 \times 64$  dimensional noise input  $z$  to the measurement information  $y$  of the same shape. Again,  $\lambda = 1000$  worked best, while lower values caused some random artifacts and higher values caused increasing blurriness. We did the same latent optimization as described for MNIST and Fashion-MNIST for this approach on CelebA as well.

**Results:** Table 1 contains the numerical results for various metrics by the different approaches for CelebA. The plots in Figure 5 again show the reconstruction for eight test samples, where the first row contains



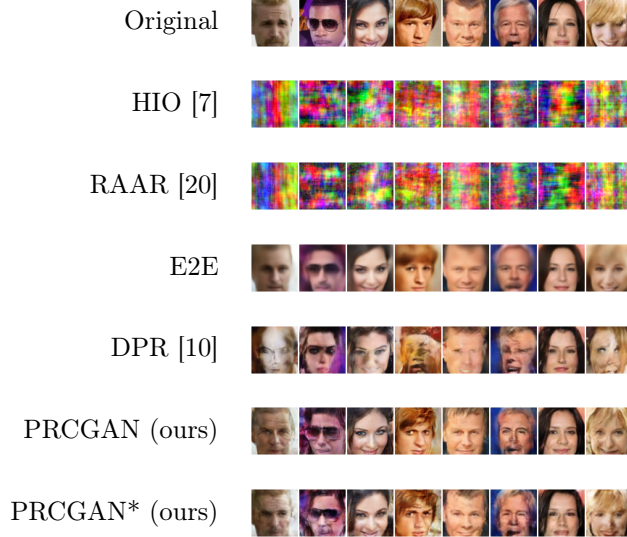


Figure 5: Reconstructions of samples from the CelebA test dataset for each model.

the original ground truth. The traditional approaches like HIO and RAAR are completely overwhelmed by this task and in contrast to MNIST and Fashion-MNIST there are not even any recognizable patterns anymore. While the DPR approach only got stuck sometimes in the optimization process with samples from MNIST and Fashion-MNIST, it now produced very distorted outputs almost all the time. The PRCGAN\* still performs best out of all approaches, although the lead over the E2E and PRCGAN approaches becomes smaller.

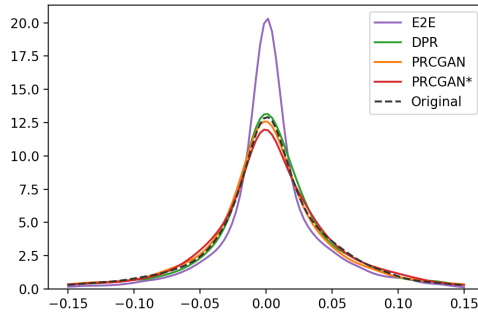


Figure 6: Distribution of the image gradients for various reconstruction methods on an image from the CelebA test dataset.

While E2E outperforms PRCGAN in all evaluation metrics, it produces very blurry outputs. The human eye can easily distinguish between the original and generated images from E2E. The PRCGAN produces much more natural looking outputs. Figure 6 shows the empirical density of the image gradient’s magnitudes from an image of the CelebA test dataset. We can observe that the E2E approach pushes the distribution of the gradients towards zero, i.e., it tends to remove edges. Our PRCGAN and the PRCGAN\*, as well as the DPR approach, preserve the distribution of the edges.

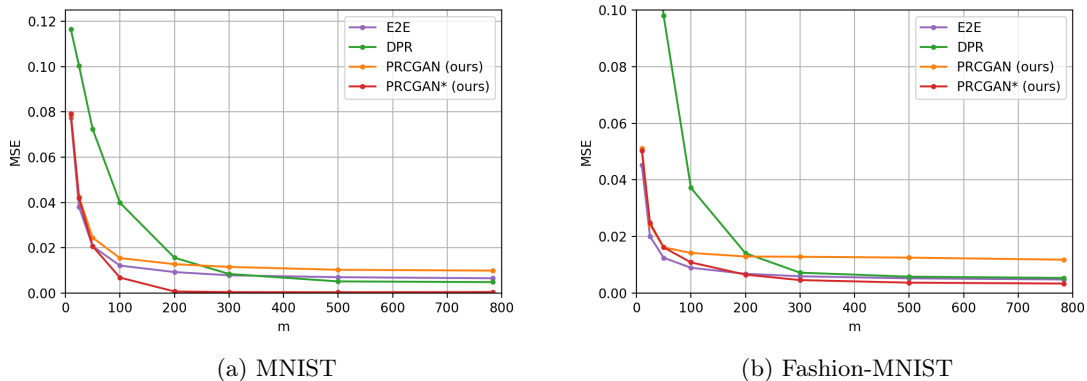


Figure 7: Comparison of the PRCGAN, the E2E and generative prior approaches for different numbers of measurements  $m$ .

## 4 Experiments: Compressive Phase Retrieval

For a next experiment we compared our PRCGAN approach to the DPR approach on the compressive phase retrieval problem with different amounts of information available. For measurements we take a Gaussian measurement matrix  $A \in \mathbb{R}^{m \times n}$ , where  $A$  has random entries sampled from  $\mathcal{N}(0, 1/m)$ . While for Fourier phase retrieval with a fixed measurement matrix  $\mathcal{F}$  our only choice to conduct a harder experiment was to use harder dataset conditions, we can now smoothly adjust the hardness of reconstruction by increasing the number of measurements  $m$ . Knowledge of the measurement matrix  $A$ , that we kept fixed for each choice of  $m$ , allowed us to use the measurements  $y$  also for the training of our PRCGAN model. For this experiment we took the same MNIST and Fashion-MNIST datasets and the same model structures for the PRCGAN and VAE as described in Section 3.1. Since for MNIST a latent space of 20 worked better for the VAE in the Gaussian measurement case, this was our only replacement in the model structure.

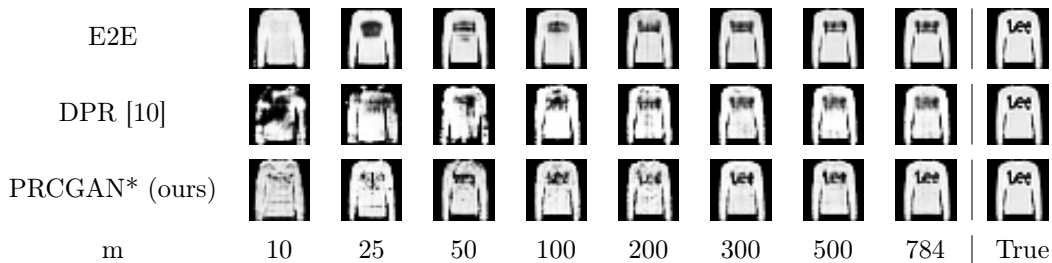


Figure 8: Reconstructions of an Fashion-MNIST test image for a varying number of measurements  $m$ .

Figure 7 shows the results for different values for  $m$ , where the maximum  $m$  was chosen as  $m = n$ . Higher values for  $m$  are possible, but we do not expect better results, since Figure 7 shows that there is barely a difference between the reconstruction error for 500 and 784 measurements. As evaluation metric we chose the MSE. Since the Gaussian measurements are not invariant under translation or 180 degree rotations as for the Fourier measurements, no image registration was needed for this experiment. First, we report the results for the DPR approach, where we optimized the latent space of the VAE to minimize the measurement error. Next, we evaluate the PRCGAN and E2E approach, where we trained a new model for each value of  $m$ . For PRCGAN\* we additionally optimized the latent variable input for the PRCGAN models. Both plots show that lowering the measurement size increases the reconstruction error for all approaches. Among

both approaches with latent optimization our PRCGAN\* outperforms the DPR approach for all sizes of measurements. DPR is strongly influenced by a smaller measurement size. While PRCGAN without latent optimization showed the worst performance for high amounts of information available, it is most robust to lowering the measurement size. While PRCGAN\* performs best for almost all sizes of measurements, E2E becomes the leading approach for the very small measurement sizes. However, we attribute this to the consistent pixel wise risk minimization in contrast to the overall reconstruction quality. Figure 8 shows the reconstructions of the different methods for a varying number of measurements  $m$ . Even for a quite small number of measurements, e.g.,  $m=200$ , the PRCGAN\* approach succeeded in reconstructing the lettering on the sweatshirt, while the other methods, in particular the E2E, fail to do so.

## 5 Limitations

We also evaluate our PRCGAN\* on the CIFAR-10 dataset and observe that our approach fails this dataset. This could be caused by the high variance of the images in the dataset. The results are shown in Figure 9.

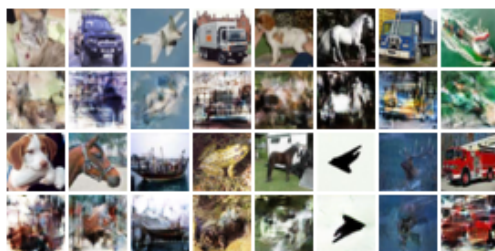


Figure 9: Original images of the CIFAR-10 dataset and unregistered reconstructions of our PRCGAN\*. Odd rows contain original images, whereas even rows contain the reconstructions.

## 6 Conclusion

Our experiments show that incorporating knowledge of the measurement matrix into the training process can improve the reconstruction quality. Even when training on perfect, synthetic measurements our model is still very robust to noise. Our conditional GAN approach yields smaller errors while still providing sharp images unlike the end-to-end approach. The drawback of our method is the fact that changing the measurement matrix requires retraining the model.

## References

- [1] Lokesh Boominathan, Mayug Maniparambil, Honey Gupta, Rahul Baburajan, and Kaushik Mitra. Phase retrieval for fourier ptychography under varying amount of measurements. *arXiv preprint arXiv:1805.03593*, 2018.
- [2] Lisa Gottesfeld Brown. A survey of image registration techniques. *ACM computing surveys (CSUR)*, 24(4):325–376, 1992.
- [3] T Tony Cai, Xiaodong Li, Zongming Ma, et al. Optimal rates of convergence for noisy sparse phase retrieval via thresholded wirtinger flow. *The Annals of Statistics*, 44(5):2221–2251, 2016.
- [4] Emmanuel J Candes, Xiaodong Li, and Mahdi Soltanolkotabi. Phase retrieval via wirtinger flow: Theory and algorithms. *IEEE Transactions on Information Theory*, 61(4):1985–2007, 2015.

- [5] Veit Elser, Ti-Yen Lan, and Tamir Bendory. Benchmark problems for phase retrieval. *SIAM Journal on Imaging Sciences*, 11(4):2429–2455, 2018.
- [6] C Fienup and J Dainty. Phase retrieval and image reconstruction for astronomy. *Image recovery: theory and application*, 231:275, 1987.
- [7] James R Fienup. Phase retrieval algorithms: a comparison. *Applied optics*, 21(15):2758–2769, 1982.
- [8] Ralph W Gerchberg. A practical algorithm for the determination of phase from image and diffraction plane pictures. *Optik*, 35:237–246, 1972.
- [9] Ian Goodfellow, Jean Pouget-Abadie, Mehdi Mirza, Bing Xu, David Warde-Farley, Sherjil Ozair, Aaron Courville, and Yoshua Bengio. Generative adversarial nets. In *Advances in neural information processing systems*, pages 2672–2680, 2014.
- [10] Paul Hand, Oscar Leong, and Vladislav Voroninski. Phase retrieval under a generative prior. *CoRR*, abs/1807.04261, 2018.
- [11] Sergey Ioffe and Christian Szegedy. Batch normalization: Accelerating deep network training by reducing internal covariate shift. *arXiv preprint arXiv:1502.03167*, 2015.
- [12] Çağatay Işıl, Figen S Oktem, and Aykut Koç. Deep iterative reconstruction for phase retrieval. *arXiv preprint arXiv:1904.11301*, 2019.
- [13] Phillip Isola, Jun-Yan Zhu, Tinghui Zhou, and Alexei A Efros. Image-to-image translation with conditional adversarial networks. In *Proceedings of the IEEE conference on computer vision and pattern recognition*, pages 1125–1134, 2017.
- [14] Kishore Jaganathan, Samet Oymak, and Babak Hassibi. Sparse phase retrieval: Convex algorithms and limitations. In *2013 IEEE International Symposium on Information Theory*, pages 1022–1026. IEEE, 2013.
- [15] Diederik P Kingma and Jimmy Ba. Adam: A method for stochastic optimization. *arXiv preprint arXiv:1412.6980*, 2014.
- [16] Diederik P Kingma and Max Welling. Auto-encoding variational bayes. *arXiv preprint arXiv:1312.6114*, 2013.
- [17] Tatiana Latychevskaja. Iterative phase retrieval in coherent diffractive imaging: practical issues. *Applied optics*, 57(25):7187–7197, 2018.
- [18] Yann LeCun, Léon Bottou, Yoshua Bengio, Patrick Haffner, et al. Gradient-based learning applied to document recognition. *Proceedings of the IEEE*, 86(11):2278–2324, 1998.
- [19] Ziwei Liu, Ping Luo, Xiaogang Wang, and Xiaoou Tang. Deep learning face attributes in the wild. In *Proceedings of the IEEE international conference on computer vision*, pages 3730–3738, 2015.
- [20] D Russell Luke. Relaxed averaged alternating reflections for diffraction imaging. *Inverse problems*, 21(1):37–50, 2005.
- [21] Xudong Mao, Qing Li, Haoran Xie, Raymond YK Lau, Zhen Wang, and Stephen Paul Smolley. Least squares generative adversarial networks. In *Proceedings of the IEEE International Conference on Computer Vision*, pages 2794–2802, 2017.
- [22] Michael Mathieu, Camille Couprie, and Yann LeCun. Deep multi-scale video prediction beyond mean square error. *arXiv preprint arXiv:1511.05440*, 2015.

- [23] Christopher A Metzler, Philip Schniter, Ashok Veeraraghavan, and Richard G Baraniuk. prdeep: Robust phase retrieval with a flexible deep network. *arXiv preprint arXiv:1803.00212*, 2018.
- [24] Jianwei Miao, David Sayre, and HN Chapman. Phase retrieval from the magnitude of the fourier transforms of nonperiodic objects. *JOSA A*, 15(6):1662–1669, 1998.
- [25] Rick P Millane. Phase retrieval in crystallography and optics. *JOSA A*, 7(3):394–411, 1990.
- [26] Mehdi Mirza and Simon Osindero. Conditional generative adversarial nets. *arXiv preprint arXiv:1411.1784*, 2014.
- [27] Henrik Ohlsson, Allen Yang, Roy Dong, and Shankar Sastry. Cprl – an extension of compressive sensing to the phase retrieval problem. In F. Pereira, C. J. C. Burges, L. Bottou, and K. Q. Weinberger, editors, *Advances in Neural Information Processing Systems 25*, pages 1367–1375. Curran Associates, Inc., 2012.
- [28] Deepak Pathak, Philipp Krahenbuhl, Jeff Donahue, Trevor Darrell, and Alexei A Efros. Context encoders: Feature learning by inpainting. In *Proceedings of the IEEE conference on computer vision and pattern recognition*, pages 2536–2544, 2016.
- [29] Alec Radford, Luke Metz, and Soumith Chintala. Unsupervised representation learning with deep convolutional generative adversarial networks. *arXiv preprint arXiv:1511.06434*, 2015.
- [30] Andreas M Tillmann, Yonina C Eldar, and Julien Mairal. Dolphin dictionary learning for phase retrieval. *IEEE Transactions on Signal Processing*, 64(24):6485–6500, 2016.
- [31] Zhou Wang and Alan C Bovik. Mean squared error: Love it or leave it? a new look at signal fidelity measures. *IEEE signal processing magazine*, 26(1):98–117, 2009.
- [32] Zhou Wang, Alan C Bovik, Hamid R Sheikh, Eero P Simoncelli, et al. Image quality assessment: from error visibility to structural similarity. *IEEE transactions on image processing*, 13(4):600–612, 2004.
- [33] Han Xiao, Kashif Rasul, and Roland Vollgraf. Fashion-mnist: a novel image dataset for benchmarking machine learning algorithms. 2017.
- [34] Li-Hao Yeh, Jonathan Dong, Jingshan Zhong, Lei Tian, Michael Chen, Gongguo Tang, Mahdi Soltanolkotabi, and Laura Waller. Experimental robustness of fourier ptychography phase retrieval algorithms. *Optics express*, 23(26):33214–33240, 2015.
- [35] Guoan Zheng, Roarke Horstmeyer, and Changhuei Yang. Wide-field, high-resolution fourier ptychographic microscopy. *Nature photonics*, 7(9):739, 2013.